**University of Alberta**

# *Evolution of a Boundary Current on a Sloping Bottom in a Rotating Fluid*

by

*Mehdi Saghafi*

A thesis submitted to the Faculty of Graduate Studies and Research in partial fulfillment of the requirements for the degree of *Master of Science*

Department of *Earth and Atmospheric Sciences*

Edmonton, Alberta
Fall, 2004

Library and Archives Canada

Published Heritage Branch

395 Wellington Street
Ottawa ON K1A 0N4
Canada

Bibliothèque et Archives Canada

Direction du Patrimoine de l'édition

395, rue Wellington
Ottawa ON K1A 0N4
Canada

*Your file Votre référence*
*ISBN: 0-612-95846-9*
*Our file Notre référence*
*ISBN: 0-612-95846-9*

The author has granted a non-exclusive license allowing the Library and Archives Canada to reproduce, loan, distribute or sell copies of this thesis in microform, paper or electronic formats.

The author retains ownership of the copyright in this thesis. Neither the thesis nor substantial extracts from it may be printed or otherwise reproduced without the author's permission.

L'auteur a accordé une licence non exclusive permettant à la Bibliothèque et Archives Canada de reproduire, prêter, distribuer ou vendre des copies de cette thèse sous la forme de microfiche/film, de reproduction sur papier ou sur format électronique.

L'auteur conserve la propriété du droit d'auteur qui protège cette thèse. Ni la thèse ni des extraits substantiels de celle-ci ne doivent être imprimés ou aturement reproduits sans son autorisation.

---

In compliance with the Canadian Privacy Act some supporting forms may have been removed from this thesis.

While these forms may be included in the document page count, their removal does not represent any loss of content from the thesis.

Conformément à la loi canadienne sur la protection de la vie privée, quelques formulaires secondaires ont été enlevés de cette thèse.

Bien que ces formulaires aient inclus dans la pagination, il n'y aura aucun contenu manquant.

Canada

# Dedication

**To the memories of my father and brother and to my family.**

# Acknowledgments

I express my deepest gratitude to my supervisors, Professor Andrew Bush and Professor Bruce Sutherland for their meticulous edits of my thesis and the efforts that they put in my research. I specially thank the Examining Committee, Professor Moodie, Professor Swaters and Professor Myers for their valuable comments on my thesis.

# Contents


**1 Introduction** **1**

**2 Experimental set-up** **10**

2.1 Tank set-up and rotation . . . . . 11

2.2 Fluid injection . . . . . 18

2.2.1 First series . . . . . 18

2.2.2 Second series . . . . . 20

2.3 Visualization and digital analysis . . . . . 22

**3 Qualitative results** **26**

3.1 First series (Barotropic mode) . . . . . 26

3.1.1 Basic fluid motion patterns . . . . . 27

3.1.2 Replication of ST58 . . . . . 35

3.2 Second series (Baroclinic mode) . . . . . 37

3.2.1 Basic fluid motion patterns . . . . . 38

3.2.2 Impact of $m_b$, $A_n$ and $H_T$ on the flow pattern . . . . . 41

**4 Quantitative results** **42**

4.1 First series . . . . . 42

4.2 Second series . . . . . 45

**5 Conclusions** **52**

**Bibliography** **55**

**List of Tables**

Table 3.1: Quasi-steady cases. ..... Page 29

Table 3.2: Unsteady cases. ..... Page 31

**List of Figures**

Figure 2.1: A photograph of the apparatus used for the experiments. Page 11

Figure 2.2: Experimental set-up. ..... Page 13

Figure 2.3: Line segments AB (2 cm from the western wall) and CD (C is 30 cm from the apex) intersect the boundary flow. ..... Page 23

Figure 2.4: Along and across-boundary time series taken along line segments AB and CD respectively. ..... Page 24

Figure 2.5: Snapshots from the side camera showing the dome-shaped eddies advancing along the western wall. ..... Page 25

Figure 3.1: An example of quasi-steady flow pattern. ..... Page 30

Figure 3.2: An example of unsteady flow pattern. ..... Page 32

Figure 3.3: Examples of flow patterns when the source was placed in 6 cm from the source. ..... Page 33

Figure 3.4: Examples of flow patterns when the source was placed in 55 cm from the source. ..... Page 35

Figure 3.5: Time series taken from the experiment in which the ST58 work was replicated. ..... Page 37

Figure 3.6: Snapshots from a reference experiment with a flow pattern consisted of an eddies train. ..... Page 39

Figure 4.1: Nondimensional boundary current velocity versus $\lambda$. ..... Page 43

Figure 4.2: Nondimensional boundary current width versus $\lambda$. ..... Page 44

Figure 4.3: Nondimensional eddy velocity versus $\lambda'$. ..... Page 46

Figure 4.4: Nondimensional eddy radius versus $\lambda'$. ..... Page 47

Figure 4.5: Boundary current and eddy propagation velocities versus Coriolis parameter, $f$. ..... Page 48

Figure 4.6: Eddy radius scaled by $R_n$ versus $\lambda_n$. ..... Page 50

Figure 4.7: Eddy velocity scaled by $U_n$ versus $\lambda_n$. ..... Page 51

**Nomenclature**

$f$ Coriolis parameter

$g'$ reduced gravity

$H_T$ maximum depth of unperturbed ambient fluid

$S$ source strength

$A_n$ nozzle surface area

$m_b$ bottom slope

$U_b$ boundary current velocity

$W_b$ boundary current width

$U_e$ eddy velocity

$r_e$ eddy size

$L$ length scale (barotropic)

$L_D$ length scale (baroclinic)

$\beta$ variation of the Coriolis parameter with latitude

$g$ Earth gravitational acceleration

$\Omega$ rotation rate

$\theta$ apex angle

$a$ tank radius

$r$ distance from the axis of the rotation

$H_d$ dense flow maximum depth

$\tau_b$ time scale associated with $\beta$

$\tau_v$ time scale associated with vortex formation

$\lambda$ nondimensional parameter (barotropic)

$\lambda'$ nondimensional parameter (baroclinic)

$\lambda_n$ nondimensional parameter (N02)

$R_n$ eddy size (N02)

$c_n$ Nof speed

$P$ potential vorticity

# Chapter 1

# Introduction

At high latitudes, the surface layer of the ocean loses both sensible and latent heat to the atmosphere. When this loss occurs rapidly, such as during exposure to extremely cold Arctic air, surface waters become denser than the subsurface waters and therefore convective overturning can occur. In the North Atlantic, this convectively formed deep water flows southward as an abyssal branch of the thermohaline circulation. Various dynamical processes act on this water mass (Gill 1982).

As an example, cold dense water in the Greenland Sea sinks to the bottom of the Atlantic. It then, moves southwards along the western boundary until it reaches the Antarctic Circumpolar Current (ACC). There it meets deep water formed in the Weddell Sea. From here it enters the Indian and Pacific oceans then it slowly upwells towards the surface, and begins returning to the

Atlantic. In the Atlantic, it returns to the Greenland Sea *via* Gulf Stream, a process which takes a few thousands years. Hence the northward flow of the thermohaline circulation in Atlantic Ocean enhances the Gulf Stream whereas its southward flow weakens the Brazil Current (Broecker 1991). Hence more heat is transported northward and as a consequence the North Atlantic ocean is warmer than the South Atlantic. This creates a net transport of heat from the southern hemisphere to the northern hemisphere, and a net transport of fresh water in the opposite direction. This shows that how theromohaline circulation affects the climate.

A general picture of the wind-driven, surface circulation is that broad, anticyclonic gyres circulate around the ocean basins exhibiting narrow and strong western boundary currents. A simplified picture of the overturning thermohaline circulation is that water sinks primarily in high northern latitudes, flows into the southern hemisphere, somehow returns to the surface where it is carried back to high northern latitudes by surface currents. These two circulations must be coupled to conserve mass in the ocean but because they act on very different timescales, how they are coupled remains an unanswered question (Pedlosky, 1996). The problem lies in our lack of knowledge about the upwelling processes that govern vertical mixing in the abyssal ocean. This mixing has traditionally been assumed to be diffusive (Stommel and Arons, 1960) for mathematical (and numerical) simplicity but is now being linked to the dynamics of internal wave breaking (Ledwell et al, 1993, Polzin et al., 1997, Killworth 1998, Egbert and

Ray ,2000 among others). It follows that the governing dynamics of each region is different.

In most theories of the gyre circulation, the vertical structure of the ocean is not considered, and the resulting circulation is purely horizontal. It is clear, however, that the circulation spans multiple spatial scales. There are the large, $O(1000)$ km gyres in the interior of the ocean basins and there are much smaller, $O(100)$ km western boundary currents that exhibit much faster velocities. Hence we expect different dynamics in these two different regions (boundary and interior) which must be merged smoothly in order to form a consistent theory of the overall gyre circulation. The first theory for the interior circulation was developed by Sverdrup in 1947 and still remains our basic framework for theoretical work on the gyre circulation (Pedlosky, 1996).

The Sverdrup theory deals only with the ocean interior and excludes western boundary currents and the thermohaline circulation. By making the geostrophic and incompressibility assumptions and neglecting bottom friction, he solved the horizontal momentum equations for a flat bottomed, homogeneous ocean. The meridional velocity is thereby given as (e.g., Pedlosky, 1996):

$$\beta v = f\frac{\partial w}{\partial z}, \tag{1.1}$$

where $\beta$ is the meridional derivative of the Coriolis parameter ($f$), $w$ is vertical velocity, and $v$ is the meridional velocity. If we integrate (1.1) with respect to $z$ over the whole water column of depth $H$ and assume that the vertical veloc-

ity vanishes at the bottom of the water column, we arrive at the fundamental expression of Sverdrup balance:

$$\beta v_s \equiv \beta \int_{-H}^{0} v dz = curl(\frac{\tau}{\rho_0}) \tag{1.2}$$

where $v_s$ is the depth-integrated meridional velocity, $\tau$ is the horizontal wind stress, and $\rho_0$ is the density of water which is assumed to be constant. The meridional transport is directly related to the curl of the wind stress, so the wind directly drives flow in the Ekman layer and the bulk of the ocean beneath the mixed layer is set into motion through vortex tube stretching. The vertical velocity in (1.1), although very weak, is the principal driver of flow in the bulk of the ocean. This balance is the foundation for theories of the gyre circulation.

In a series of laboratory experiments with a rotating, pie-shaped wedge, ST58 estimated mass transport in the presence of different source-sink arrays. They studied four different cases corresponding to different locations of the source(s). In the first case, a single source was placed at the apex of the wedge (which, given the tank configuration and rotation, is analogous to the high latitudes of the northern hemisphere); in the second case, the source was along the "western" wall near the "southwestern" corner; in the third case, the source was the same as in the second case but a sink of equal (but opposite) strength was placed at the apex; and in the fourth case, the source was placed along the "southeastern" wall and a sink of equal (but opposite) strength was placed near the "southeastern" corner. For all cases (except the last) they observed

an intense western boundary current flowing southward and a northward return flow in the interior with a mass transport $T_w$ estimated by:

$$T_w = -S_0 - S(\frac{2gD_0}{\Omega^2 r_0^2}), \tag{1.3}$$

in which $D_0$ is the depth of the fluid when the system is at rest, $\Omega$ is the angular velocity, $r_0$ is the radius of the tank, $g$ is the gravitational acceleration, and $S_0$ and $S$ are the source and sink strengths, respectively. In all these cases, the observed velocity in the interior is radial and directed toward the apex (i.e. is northward flowing), and its mass transport is consistent with the Sverdrup relation (1.2) (see ST58 for more detail). In the fourth case where the source is placed on the "eastern; boundary, no western boundary current formed and hence there was no radial velocity in the interior.

In order to have an experimental reference we reproduced ST58 in our slightly modified set up. We then expand upon their work by including baroclinic dynamics.

Investigating the circulation in the North Atlantic Ocean, Stommel , used the same equations used by Sverdrup with an additional bottom stress which was proportional to velocity. He then, calculated steady-state solutions for flow in a rectangular geometry of constant depth for a water of constant density. For a non-rotating Earth and rotating Earth with a constant rotation his solutions had a symmetric flow pattern with no western boundary current. For a rotating

Earth, with the Coriolis force varying with latitude, however he found a solution with western intensification (Stewart 2003). This could be explained in terms of the conservation of the potential vorticty in the subtropical gyre as well. In the eastern boundary as the flow moves southward Coriolis force decreases but this is balanced by the vorticity input by the wind (westerlies). On the other hand the planetary vorticity in the west decreases as the flow moves northward and a source of vorticity must balance this decrease. It can be said that in the relative vorticity generated by shear in the western boundary current is the balancing source. Thus a western intensification occurs which is the origin of the western boundary current. The boundary currents formed in this way play an important role in the overall thermohaline circulation pattern in the North Atlantic Ocean. Labrador current, Gulf stream and Brazil current can be considered as a result of this western intensification.

To find a model of western boundary flow which is consistent with the interior model of Sverdrup, the boundary layer problem must be solved in a way that satisfies all the necessary boundary conditions. Munk (1950) excluded nonlinearity (which is equivalent to prescribing small Reynolds number or large viscosity) and bottom friction from the boundary layer equation. He also ignored vertical motion. The resulting circulation in the interior of the basin was of the Sverdrup type which returned *via* northward flow in a western boundary current. Munk's linear model, although not a particularly realistic model (Pedlosky 1987) was nevertheless the first attempt to unify the dynamics of the western boundary

layer and the interior of the ocean. A relevant length scale (for boundary flow width) in Munk's model is, $\delta_M = \sqrt[3]{\frac{A_H}{\beta}}$, where $A_H$ is the horizontal turbulent viscosity coefficient.

Whereas Munk (1950) formulated his model in the limit of small Reynolds number, Morgan (1956) postulated a purely inertial model in the limits of large Reynolds number (where viscosity does not play an important role). He found a solution for boundary layer flow by conserving the potential vorticity only on the western boundary region. But this solution failed to join the Sverdrup interior solution. The relevant length scale for boundary current width in his model was $\delta_M = \sqrt{\frac{U}{\beta}}$ where $U$ is the speed of the boundary current.

In an attempt to modify Munk's linear model, Ierley (1987) kept the non-linear terms in the vorticity equation and solved the problem numerically. The simple physical concept behind his model was that the complete circulation is the sum of a Sverdrup interior and a boundary layer near the western boundary. His results, however, failed to satisfy the classical and basic boundary layer condition which is $\frac{\partial}{\partial x} \gg \frac{\partial}{\partial y}$ (see Ierely 1987 for more detail).

There have been other attempts to find a consistent solution that joins the boundary flow to the interior flow (Ierley and Reuher, 1986; Hendershott, 1987; Cessi et al. 1990; Ierley and Sheremet, 1995 among others) but while these efforts managed to solve some aspects of the problem they could not provide a consistent model by which this dynamical duality (between boundary current

and interior) may be addressed.

The evolution of the benthic boundary current is of great importance to contemporary oceanography. In many circumstances eddies are developed and carry the isolated water mass from higher latitudes to lower latitudes over few thousands of kilometers (Nof, 1983). Hence the eddy formation mechanisms have received considerable attention in the recent oceanographic literature. Different mechanisms for eddy formation are proposed by Griffith et al. (1982), Swaters (1991), Condie (1995) and Reszka et al. (2002) all of which suppose that baroclinic instability plays an important role. Swaters (1991) introduces an interaction parameter, $\mu$, which may be used as an index of instability growth in the flow. This parameter is a measure of the ratio of the destabilizing effect of an eddy's thickness (or vortex stretching) to the stabilizing effect of the basin bottom slope. On the other hand, N02 in investigating the origin of Reddy (intermediate eddies form in the Red Sea) formation, suggest that the varying bottom topography of the Red Sea reaches a critical slope on which the flow can only exist as a train of eddies. N02 conclude that baroclinic instability does not play an important role in the formation of Reddies since mathematically no outflow current can exist to undergo baroclinic instability. Lanes-Serff and Baines (1998) (LB98 hereafter) in an experimental study, argue against the instability mechanism proposed by Swaters (1991). In their investigation they describe the eddy formation as a combined effect of viscous Ekman drainage and vortex stretching in the vicinity of the source. They examine some flow characteristics

versus the interaction parameter, $\mu$, and, since they find no significant correlation between them, they conclude that $\mu$ is not of consideration in regard to eddy formation in their experiments. In recent work, Cenedese et al. (2003) studied mixing in three different regimes (laminar, wave, eddy). In their work eddies are formed in flows with Froude numbers smaller than unity as a result of vortex stretching and Ekman dynamics.

The primary motivation for this study is to contribute to the unification of the dynamics of western boundary current and the interior flow by investigating in detail the benthic boundary current flow characteristics such as width and velocity in two different flow regimes: barotropic (homogenous) and baroclinic (two-layered). In the barotropic regime we made a comparison with ST58 and found some similar and some novel results. In each regime we found the appropriate length and velocity scales that best describe the flow, thereby adding to our knowledge of the dynamics of the benthic boundary currents on a sloping bottom.

The outline of the thesis is as follows:

In Chapter 2 we describe the experimental set-up. Flow types classification is discussed in a qualitative analysis presented in Chapter 3. In a quantitative analysis the appropriate scales for flow characteristics is discussed in Chapter 4 and, finally, in Chapter 5 concluding remarks are presented.

# Chapter 2

# Experimental set-up

All the experiments were performed in EIFL, the Environmental and Industrial Fluid Dynamics Laboratory at the University of Alberta. A total of 65 experiments were done. These experiments were subdivided into two series based on the relevant dynamics. The first series was designed to study the flow pattern of injected fluid that had the same density as ambient water that was in a rotating tank with a sloped bottom. The set-up was designed to be as similar as possible to that of ST58 and so allowed us to compare and contrast our work with theirs. In the second series of experiments, the injected fluid was denser than the ambient fluid through the addition of salt. These experiments thus extended the work of ST58 to include some of the dynamical aspects of baroclinic currents such as the deep currents in the North Atlantic Ocean.

## 2.1 Tank set-up and rotation

Figure 2.1 shows a photograph of the experimental set-up. It shows the tank on a rotating table with the surrounding superstructure. Figures 2.2a and 2.2b, respectively, show schematics of the top view and the side view of the experimental set-up. Figure 2.2a shows additional components used for the second series of experiments, including the salt water reservoir, the fresh water bucket and the angled mirror.

Figure 2.1: A photograph of the apparatus used for the experiments.

A Plexiglas cylindrical tank was centred on the rotating table. The inner radius of the tank was 45 cm and its height was 30 cm. The tank was tilted by inserting plastofoam blocks under the apex, so that the bottom slope, measured as the ratio of the height of the blocks to the diameter of the tank, was typically 0.033 in the first series and 0.13 in the second series of experiments. Sensitivity tests changed this value in each series however. Following ST58, fluid motions were established and analyzed in a pie-shaped sector, with an apex angle of 60° (Fig. 2.2a). The 30 cm tall walls of the sector were made of clear Plexiglas.

Although in ST58 the apex of the sector was placed at the centre of the rotating table, in the present work it was placed at the perimeter of the tank to provide longer sidewalls. The length of each sidewall in ST58 was approximately 1 m, but was 60 cm in the present work. Consistent with ST58, at the top part of the sector, 14 cm from the apex, was a 30 cm Plexiglas plate, positioned across the apex from one sidewall to the other as illustrated in Fig. 2.2a. The tip of the nozzle that injected fluid was positioned in the centre of this plate 6 cm from the bottom of the tank. The walls and the plate were sealed using electrical tape and plasticine to inhibit the leaking of fluid from, or into, the pie-shaped sector. The tank was covered by a Plexiglas lid to minimize the surface convection resulting from evaporation (Voropayev et al. 1997).

(a) Top view

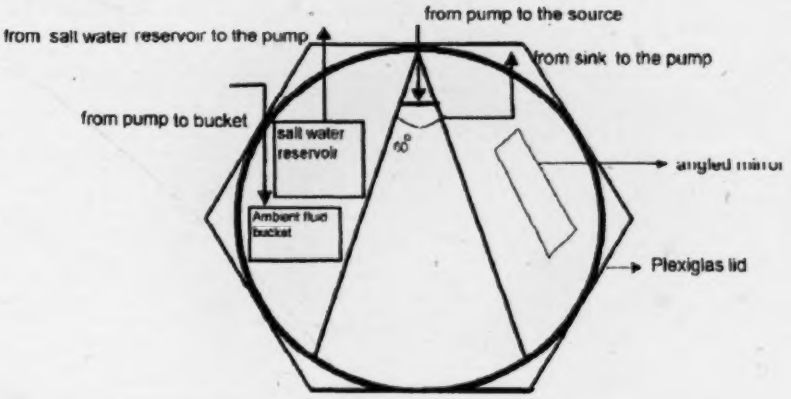


(b) Side view

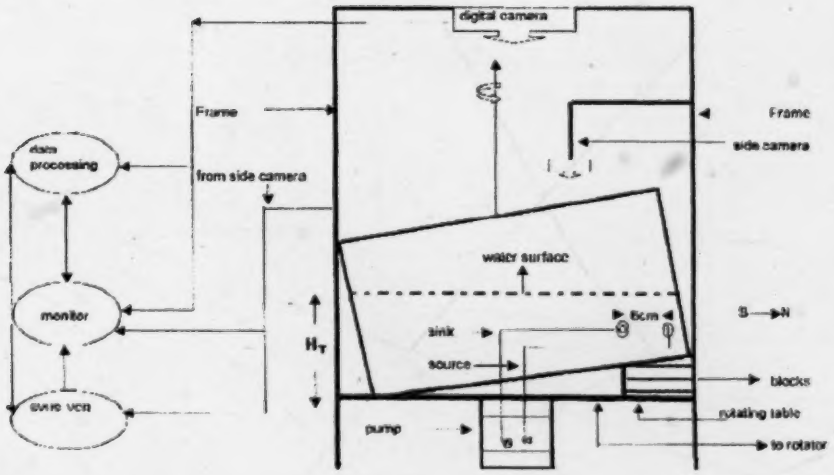


Figure 2.2: Experimental set-up. Bucket and reservoir and angled mirror were added for the second series of the experiments.

The tank was filled with fresh water to a depth of $H_T$ at the deepest part of the tank, which was typically 13 cm in the first series and 17 cm in the second series of experiments. The volume of water in this pie shaped sector can be approximated as a function of experimental parameters as

$$V_b(H_T, a, m_b, \theta) \approx a^2(\theta + \sin(\theta))(H_T - am_b). \tag{2.1}$$

where $a$ is the radius of the tank, $m_b$ is the bottom slope and $\theta$ is the apex angle of the sector.

The tank was mounted on a rotating table made by Australian Scientific Instruments. The table rotated at frequencies $\Omega$ between 0.05 and 10 $s^{-1}$ with errors of less than 0.5%. The typical range of rotation rate in the first series was between, $\Omega = 0.25$ and 1.6 $s^{-1}$ and between 0.1 and 0.5 $s^{-1}$ for the second series. The reason for using a lower range of $\Omega$ for the second series will be explained later in this section.

For these experiments it was necessary to have the ambient fluid in the tank in solid body rotation. In order to determine when solid body rotation was achieved, neutrally buoyant particles were spread on the free surface of the water and when there were no radial displacements in the particles' positions, as determined by Digimage software which is especially designed for analyzing laboratory studies of geophysical fluid dynamics (see Dalziel, 1993 for more detail), it was then determined that the water in the tank was in solid body rotation. For a rotation rate of $\Omega$= 0.5 $s^{-1}$ and a depth of $H_T$, 13 cm (at the

deepest part of the tank), the time to reach solid body rotation was about 15 minutes. It was longer for slower rotation rates and greater depths.

In a fluid rotating at an angular velocity of $\Omega$, the displacement of the free surface, $\eta$, at a radial distance, $r$, from the axis of rotation is

$$\eta = \eta_0 + \frac{\Omega^2 r^2}{2g}, \tag{2.2}$$

where, $\eta_0 = \frac{\Omega^2 a^2}{4g}$, is the change (drop) in the depth of the free surface, at $r = 0$, after solid body rotation is achieved (see Streeter (1971) for a more detailed discussion) and $g$ is the gravitational acceleration. From (2.2) the greatest depth of water in the rotating tank is

$$H = H_0 + \frac{\Omega^2 a^2}{2g}, \tag{2.3}$$

where $H_0$ is the depth of water at the centre of the tank when it is rotating. When the tank is rotating the change of the maximum depth of water, $H_T$, with respect to $H_0$, is given by the second term on the right side of (2.3).

The slope of the free surface, $m_s$, of the water due to rotation is calculated by taking the derivative of (2.2) with respect to $r$:

$$\partial\eta/\partial r \equiv m_s = r\Omega^2/g. \tag{2.4}$$

In the real ocean when an eddy moves southward in the northern hemisphere, it experiences a reduction in the planetary vorticity and therefore, by conservation of absolute vorticity, its relative vorticity increases. The same effect is produced if the eddy moves down a sloping bottom because of vortex

stretching (Niiler et al. 1987). This effect is called the topographic-$\beta$ effect. In the present work the bottom slope was used to generate a topographic-$\beta$ effect. In the present set-up, the apex resembled the north pole, the wall to its right (when looking toward the south) was the western wall (simulating the western boundary in the North Atlantic Ocean), and the wall to the left was eastern wall.

Since the range of rotation rates in the first series was fairly large, the corresponding range of displacement in the free surface of the water was large as well. In most cases the displacement of the free surface caused by rotation was greater than the change in depth due to the bottom slope. This made the topography of the water surface complicated. The depth of the water column was set by a combination of the parabolic surface deflection (caused by rotation) and the linear bottom slope (see LB98 for instance).

From (2.4) the range of maximum slope of the free surface at $r = a$ for the first series of experiments was between 0.003 and 0.118, which corresponded to a range of displacement $\Delta H_T$ of the free surface from 0.07 to 2.65 cm, respectively. For comparison the displacement caused by the bottom slope was approximately 1.5 cm.

From (2.4) it is readily seen that $m_s$ is radially dependent and since we wanted the variation negligibly small, an upper bound was imposed on the rotation rate to ensure that the maximum slope of the free surface was always

smaller than the bottom slope $m_b$. The range of $m_s$ for the second series was between 0.0005 and 0.0113 which corresponded to a range of $\Delta H_T$ from 0.01 to 0.25 cm, while the displacement caused by the bottom slope was approximately 6 cm. ST58 used (2.4) to simulate the $\beta$-plane, but we note that their $\beta$ is therefore radially dependent.

A mean value for the topographic-$\beta$ can be approximated by

$$\beta = f m_b / H, \tag{2.5}$$

where $f = 2\Omega$ is the Coriolis parameter and $H$ is the mean depth of the water in the tank (see Pedlosky (1987) for a derivation of (2.5)). In the present work, nondimensionalized quantities are used in our analysis. In doing so a nondimensional topographic-$\beta$, $\hat{\beta} = \frac{\beta L^2}{U} = (\frac{L}{L_R})^2$, is defined, where $L_R = (\frac{U}{\beta})^{1/2}$ is the "Rhines scale" (Rhines, 1975), $L$ is a length scale and $U$ is a velocity scale. A typical value for the experimental $\hat{\beta}$, taking $U$ of order $10^{-1}$ cm s$^{-1}$, (based on a typical value for the velocity of the boundary current), and $L$ of order 10 cm (based on a typical value for the width of the boundary current and eddy radius), was of order 10 (using (2.5)). For a deep boundary current in a midlatitude ocean $U$ is of order $10^{-1}$ m s$^{-1}$ (Tansley and Marshall 2001) and a horizontal length scale, $L$, is of order $10^5$ m (Apel 1990). These values give $\hat{\beta} \simeq 10$, which has the same order of magnitude as our experimental $\hat{\beta}$.

## 2.2 Fluid injection

Fluid was injected at a source and extracted at a sink (c.f. Fig. 2.2a). The proximity of the source and sink locations was chosen to represent localized convection in the real ocean in which fluid is removed from the surface and "injected" into the depths. In the first series of experiments, in which the injected fluid had the same density as the ambient fluid, the sink was placed at different locations in order to compare the results to ST58. In the second series, dense fluid was injected, and the sink was fixed at a position close to the source. These two set-ups are described below.

### 2.2.1 First series

A recirculating, peristaltic MONOSTAT pump (model 7400012123) was used to inject fluid into and extract fluid from the tank at identical volume fluxes so that the total volume of the water in the tank was conserved during the experiment. This set-up provided an advantage over the experiments described in ST58 (shown in their Fig. 8), in which mass was not conserved since they did not extract water from the tank. The pump injected fluid at a specified rate that ranged between 1 and 1.7 $cm^3 s^{-1}$, with an accuracy of 0.001 $cm^3 s^{-1}$.

The source was placed in the Plexiglas plate positioned between the western and eastern walls (7.5 cm from each) 13 cm from the apex and 6 cm from the bottom in all the experiments. The nozzle used for injection had an inner radius

of 0.25 cm. The injected fluid from the nozzle had an injection velocity $v_n = \frac{S}{A_n}$ where $A_n$ is the nozzle surface area and $S$ is the source strength. The values of $v_n$ ranged between 5 and 8.3 $\mathrm{cm\,s^{-1}}$.

The injection hose was parallel to the bottom in all experiments. A cross hair was placed at the opening of the nozzle to make the injected fluid turbulent. This technique has the advantage that the transition from laminar to turbulent flow within the tank is prevented.

To study the effect of the source-sink distance on the flow pattern, as in ST58, the sink was placed at different distances from the source on the eastern wall. These experiments will be described in Chapter 3.

Food colouring, with a density very close to that of fresh water ($\sim$0.987g $\mathrm{cm^{-3}}$ at room temperature), was used to distinguish the injected water from the fresh water in the tank. Typically, the concentration of dye in the injected water was 1% by volume. Tubing connecting the source and the sink *via* the pump, was filled with dyed water. The total volume of the dyed fluid in the tubing was approximately 320 $\mathrm{cm^3}$. The ratio of the volume of the injected dyed fluid to the volume of the water in the sector for $H_T = 13\,\mathrm{cm}$ and $m_b = 0.033$, was approximately 0.008.

### 2.2.2 Second series

In reality, there is no horizontal distance between the "source" and the "sink", because convection generally occurs in the vertical direction. In our oceans convection occurs when cold winds flux heat from the surface of the ocean making the surface water colder and denser than the underlying water. In the Atlantic Ocean, for example, this happens in certain regions including the Labrador Sea, the Greenland Sea (Madec et al. 1996), and occasionally in the Weddell Sea (Alverson and Owens 1996). Convection, however, shows a high degree of spatial variability. Observations indicate a "patchiness" on scales of tens to hundreds of kilometers (DiBattista et al. 2002). To have more similarity between the experiments and nature, the sink was fixed at the closest horizontal distance (6 cm) from the source on the eastern wall for the second series of experiments.

Two trial experiments were done with the dense fluid in order to determine how best to set up the second series of experiments. The results of these experiments showed that, if the same set-up (as the first series) was used for the injection of the fluid (i.e. using the dyed fluid within the tubing), it would have resulted in dilution of the dense fluid, because fresh water from the "sink" end of the tubing was mixed with the dense fluid in the tubing. So in the second series the extraction process was isolated from the injection process. The dense fluid was kept in a reservoir outside the experimental domain but within the tank (see

Fig. 2.2a). From one branch of the pump dense dyed fluid was drawn from the reservoir and injected into the tank continuously during the experiment. The volume of the injected fluid, therefore, depended on the pump's flow rate, $S$, and the duration of the experiment. Simultaneously from the sink, the fresh water was extracted from the tank at the same volume flux as that of the source. The removed fresh water was kept in a container, outside the experimental domain, beside the dense fluid reservoir.

Three values of density difference were used for the injected fluid: $0.0007\,\mathrm{g\,cm^{-3}}$, $0.0035\,\mathrm{g\,cm^{-3}}$ and $0.007\,\mathrm{g\,cm^{-3}}$. Measurements regarding the weight of salt necessary for making these density differences were done using an OHAUS Portable Advanced (CT200) digital scale with an accuracy of $0.005\,\mathrm{g}$.

In the second series of experiments, the impacts of several experimental parameters on flow pattern were investigated. In doing so, one parameter of interest was changed while the other parameters were kept constant at their typical values. These parameters were:

**Nozzle surface area, $A_n$**: The nozzle used for most of the experiments had an inner radius of $0.25\,\mathrm{cm}$ (with a surface area $A_n = 0.2\mathrm{cm}^2$). Some experiments were done with a nozzle radius of $0.13$ cm (with a surface area $A_n = 0.05\mathrm{cm}^2$).

**Maximum depth, $H_T$**: In most of the experiments the maximum unperturbed depth of the water in the tank was $17\,\mathrm{cm}$. It was increased to $28$ cm in some experiments.

**Bottom slope, $m_b$:** The typical angle of the bottom slope for the second series was 7.4° corresponding to a slope of 0.13. Some experiments were done with a slope angle of 3.7° , corresponding to a slope of 0.065.

## 2.3 Visualization and digital analysis

Attached to the rotating table was a superstructure on which cameras and lighting gear were mounted. A COHU digital camera was mounted 2 meters above the centre of the tank to record the experiments. Its field of view focused on a 60 by 60 cm area, with a pixel resolution of $\frac{16}{300}\ \frac{cm}{pixel}$. Using Digimage, continuous recordings from the top camera (COHU) were converted into a series of digitized snapshots that were stored on computer disk.

The time interval between snapshots was chosen to match the time it took for one revolution of the table. For example, for a rotation rate of $\Omega = 0.5\,s^{-1}$, the time interval was $2\pi/0.5 \simeq 13\,s$.

Using the "Particle Tracking" routine in Digimage, surface circulations associated with the flow near the western wall and around the source and sink were visualized by spreading tracers on the surface of the water once it reached solid body rotation.

Playing back the recorded movie on videotape, this routine tracked each tracer, and in this way it could be found whether the circulation at the surface was cyclonic or anticyclonic.

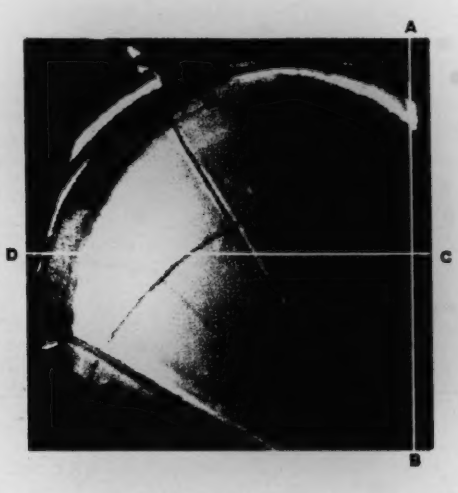


Figure 2.3: Line segments AB (2 cm from the western wall) and CD (C is 30 cm from the apex) intersect the boundary flow and were used to make along-flow and across-flow time series, respectively. In this experiment $\Delta\rho$=0, $\Omega$=1.05 $s^{-1}$, S=1.3 $cm^3 s^{-1}$, $m_b$ = 0.033 and $\Delta\rho$ is the density difference.

The velocity and width of the flow and the radius of the eddies were obtained from time series constructed from cross-sections taken through successive images of the digital movies. For example, cross sections could be taken along the flow (e.g. AB in Fig. 2.3) or across the flow (e.g. CD in Fig. 2.3). Line segments AB and CD in Fig. 2.3 were taken from the movie to make the images shown in Figures 2.4a and 2.4b, respectively. Fig. 2.4a is in fact composed of 103 vertical lines each of which is the head of the boundary current at intervals of 5.8 s (the same time interval that the snapshots had in the digitized movie). In

Fig. 2.4a, the horizontal axis shows the time, and the vertical axis shows the position of the boundary current head as it moves southward along the western wall. The boundary between dyed and undyed fluid marks the frontal advance. By finding the slope of this boundary the velocity of the head can be calculated.

Fig. 2.4b shows an across-flow time series of the same experiment. The horizontal axis shows the time and the vertical axis shows the width of the flow along line segment CD in Fig. 2.3. The average width of the current at that location could be calculated from this graph.

(a) Along-boundary time series taken along the line segment AB in Fig. 2.3.

(b) Across-flow time series taken along the line segment CD, in Fig. 2.3.

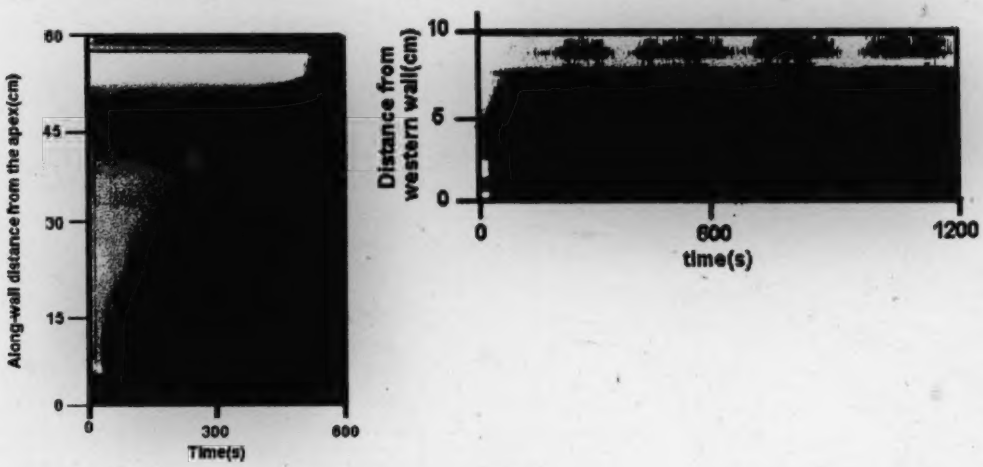


Figure 2.4: Along and across-boundary time series taken along line segments AB and CD respectively. The bright zone seen at the top part of the Fig. 2.4a is due to light reflection by the rim of the tank.

To visualize the vertical structure of the dense western boundary flow in the second series of experiments a DCR-TRV6 Sony digital video camera was mounted 80 cm above an angled mirror which was outside the eastern wall of the sector but inside the cylindrical tank. Thus the camera continuously recorded side-views of the boundary current. The images were taped on an SVHS Panasonic VCR and were later digitized using Digimage in the same way as for the top camera recordings. The dimensions of the field of view from this camera were typically 18 by 10 cm. One digitally enhanced snapshot taken from a movie recorded by the side camera is shown in Fig. 2.5.

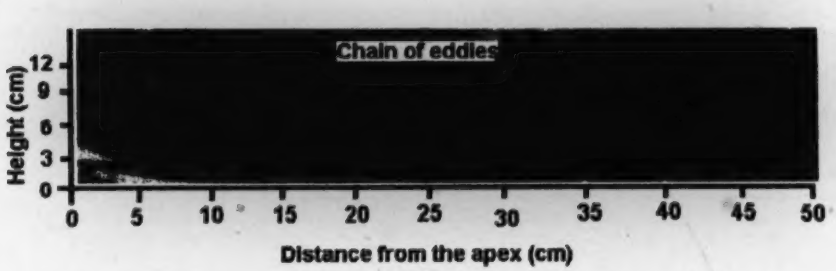


Figure 2.5: Snapshots from the side camera showing the dome-shaped eddies advancing along the western wall. In this experiment $\Delta\rho$=0.007 g $cm^{-3}$, $\Omega$=0.3 $s^{-1}$, S=0.17 $cm^3 s^{-1}$, $m_b = 0.13$.

# Chapter 3

# Qualitative results

In this chapter all the observed flow patterns are described and classified. Classification of experiments in the first series is based on a nondimensional parameter which measures the steadiness of the flow pattern.

## 3.1 First series (Barotropic mode)

In the first series of experiments, the injected fluid had the same density as that of the ambient fluid; hence, the system consisting of the injected fluid and the ambient fluid was barotropic. A total of 43 experiments, each about 40 minutes in length, were done of which 8 were discarded due to technical problems. The typical slope, $m_b$, was 0.033. In 8 of the experiments, the impact of the bottom slope on the flow pattern was investigated, and so the slope was

increased to 0.065. The source-sink distance, $d$, was typically 6 cm but was varied in sensitivity tests.

### 3.1.1 Basic fluid motion patterns

Dyed fluid was injected into the tank from the nozzle once the water in the tank was in solid body rotation. Immediately after injection, fluid deflected to the right under the influence of the Coriolis force. The fluid hit the western wall and, flowed along it, southward, forming a "boundary current." In the vicinity of the nozzle there was an anticyclonic surface circulation whereas around the sink there was a cyclonic surface circulation. These were visualized using the "Tracking" routine in Digimage. Once the boundary current reached the end of the western wall it then flowed in a zonal direction (from west to east) along the southern wall. The flow pattern, however, was highly sensitive to changes in the experimental parameters. In some cases the flow was not in steady state due to high flow rates and low rotation rates.

In the real world, there are a variety of flow regimes for boundary currents which vary from quite unsteady flow to steady flow. A main goal of the present work is to simulate these different flow regimes and to find a relation between each type and the corresponding experimental parameters. Different sets of experimental parameters were therefore incorporated in a suite of sensitivity tests; high source strength ($\geq 1.33\,\mathrm{cm^3 s^{-1}}$) with moderate rotation rate ($0.8 \leq$

$\Omega \leq 1.05\,s^{-1}$), and high source strength with low rotation rate ($0.25 \leq \Omega \leq 0.6\,s^{-1}$).

After doing all experiments, two basic flow patterns were observed. These basic patterns are defined as: quasi-steady (which was a spatially smooth and almost temporally steady flow near the western wall); unsteady (which was a flow with fast changes in shape).

To determine the dependency of each flow type on experimental parameters, we determined to find an appropriate nondimensional parameter through the physics of the phenomena. In the following we describe the process by which we managed to find this parameter.

As mentioned in Chapter 2 there is an input velocity, $v_n = \frac{S}{A_n}$, associated with the fluid injection. Upon dividing $v_n$ by $f$, a length scale, $L=\frac{v_n}{f}$, is obtained which is a measure of the size of the vortex formed near the nozzle. The volume of the vortex, $V_v$, can then be approximated as the volume of the water column which has a radius of $L$ and its height, as given by a typical scale height. Dividing $V_v$ by source strength, $S$ gives a measure of the time scale, $\tau_v$, by which the vortex is formed. Since fluid particle enters the boundary current *via* a Rossby wave mechanism, the reciprocal of the Rossby wave frequency gives an appropriate time scale, $\tau_b = (\beta L)^{-1}$, (where $\beta$ is given by (2.5)). Dividing $\tau_b$ by $\tau_v$ the following nondimensional parameter for flow classification is obtained:

$$\lambda = \frac{\tau_b}{\tau_v} = \frac{A_n^3 f^2}{S^2 m_b}. \tag{3.1}$$

We classified different flows produced in our experiments based on their corresponding values of $\lambda$. In the following we describe each flow type with its corresponding interval of $\lambda$.

| Exp. | $S(\mathrm{cm^3 s^{-1}})$ | $\Omega(\mathrm{s^{-1}})$ | $m_b$ | $\lambda$ |
|---|---|---|---|---|
| 1 | 1.50 | 0.90 | 0.065 | 0.177 |
| 2 | 1.67 | 1.00 | 0.065 | 0.177 |
| 3 | 1.67 | 0.80 | 0.033 | 0.223 |
| 4 | 1.67 | 0.85 | 0.033 | 0.252 |
| 5 | 1.33 | 1.00 | 0.065 | 0.277 |
| 6 | 1.67 | 0.90 | 0.033 | 0.283 |
| 7 | 1.67 | 0.95 | 0.033 | 0.315 |
| 8 | 1.67 | 1.00 | 0.033 | 0.349 |
| 9 | 1.50 | 1.00 | 0.033 | 0.431 |
| 10 | 1.33 | 0.90 | 0.033 | 0.442 |
| 11 | 1.00 | 1.00 | 0.065 | 0.492 |
| 12 | 1.33 | 1.00 | 0.033 | 0.545 |
| 13 | 1.67 | 1.30 | 0.033 | 0.590 |
| 14 | 1.67 | 1.40 | 0.033 | 0.684 |
| 15 | 1.17 | 1.00 | 0.033 | 0.712 |
| 16 | 1.00 | 0.90 | 0.033 | 0.785 |
| 17 | 1.67 | 1.60 | 0.033 | 0.894 |
| 18 | 1.00 | 1.00 | 0.033 | 0.970 |

Table 3.1: Quasi-steady cases. For all cases $d$=6 cm and $A_n$= 0.2 $\mathrm{cm^2}$.

### a) Quasi-steady ($0.177 \leq \lambda \leq 0.970$)

18 experiments exhibited a quasi-steady flow pattern. The sink was fixed at a distance $d$=6 cm. Table 3.1 summarizes these cases. In all cases, relatively high source strength was compensated by a high rotation rate. The typical flow pattern was a spatially smooth and steady boundary current along the western wall. In all cases, the boundary current was confined to a relatively narrow (compared to the boundary current length) region near the wall. The width of

the boundary current, once it reached its maximum extent was almost constant throughout the remainder of the experiment.

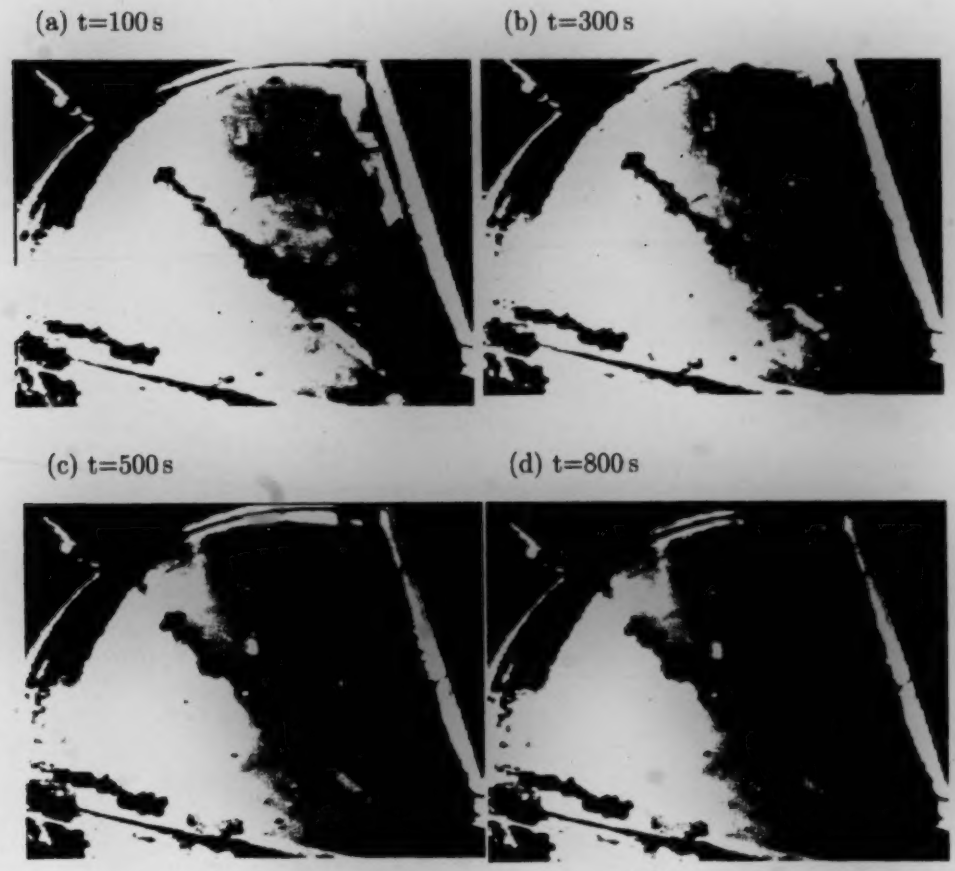


Figure 3.1: An example of quasi-steady flow. In this experiment, $\Delta\rho = 0, \Omega = 0.9\,s^{-1}$, $S = 1.67\,\mathrm{cm^3 s^{-1}}$, $m_b = 0.033$, and the source-sink distance was 6 cm.

In most cases, the current width was narrowest at the juncture of the western and southern walls and was widest near the apex. Fig. 3.1a shows the flow pattern at an early stage of the current's formation. Fig. 3.1b shows the head of

the boundary current at time $t = 300s$, as it approached the end of the western wall. At time $t = 500s$, the head of the flow had reached the southern wall (Fig. 3.1c) after which there is little temporal variability aside from the propagation of the current along the western wall (Fig. 3.1d).

**b) Unsteady ($0.022 \leq \lambda \leq 0.136$)**

7 cases are categorized as "unsteady" and are summarized in Table 3.2.

| Exp. | $S(\mathrm{cm^3 s^{-1}})$ | $\Omega(\mathrm{s^{-1}})$ | $m_b$ | $\lambda$ |
|---|---|---|---|---|
| 1 | 1.33 | 0.25 | 0.065 | 0.017 |
| 2 | 1.67 | 0.25 | 0.033 | 0.022 |
| 3 | 1.33 | 0.25 | 0.033 | 0.034 |
| 4 | 1.33 | 0.50 | 0.065 | 0.069 |
| 5 | 1.67 | 0.50 | 0.033 | 0.087 |
| 6 | 1.67 | 0.60 | 0.033 | 0.126 |
| 7 | 1.33 | 0.50 | 0.033 | 0.136 |

Table 3.2: Unsteady cases. For all cases $d$=6 cm and $A_n$= 0.2 $\mathrm{cm^2}$.

Unlike the "quasi-steady" case, the high momentum of the injected fluid was not balanced by the Coriolis force associated with high rotation rates. Values of $\lambda$ are therefore smaller for this type of flow. Unlike the quasi-steady case, a boundary current did not develop smoothly over time and was very fast ($> 0.2\,\mathrm{cm\,s^{-1}}$). The width of the flow changed rapidly with time along the western wall and was dominated by the presence of transient barotropic eddies. As a result, the flow did not develop a statistically steady spatial pattern.

In all cases, the flow was not confined to a narrow boundary region; instead, it spanned the whole tank basin. Fig. 3.2a shows an example of an "unsteady"

flow pattern, at t=300 s. Fig. 3.2b is a snapshot of this flow pattern at t=400 s. After less than 2 minutes, the change in the shape of the flow pattern was significant. Fig. 3.2c shows the flow pattern at time t=700 s, when the flow reached the southern wall. Fig. 3.2d shows the flow pattern at the t=2000 s, when the flow along the southern wall reached the eastern wall.

(a) t=300 s

(b) t=400 s

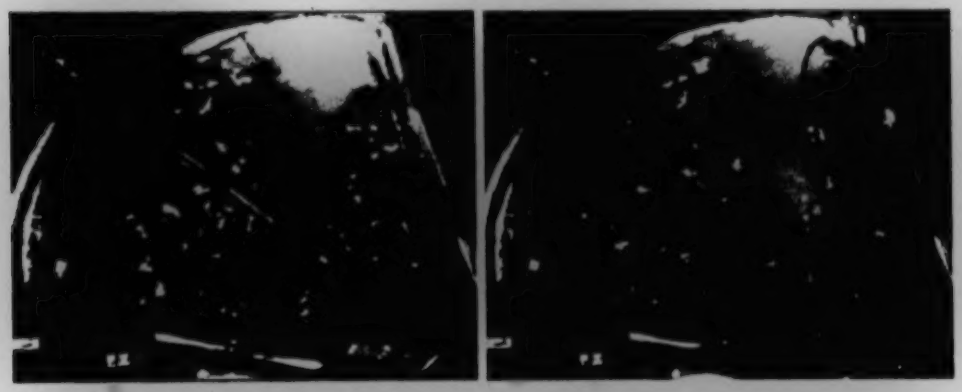

(c) t=700 s

(d) t=2000 s

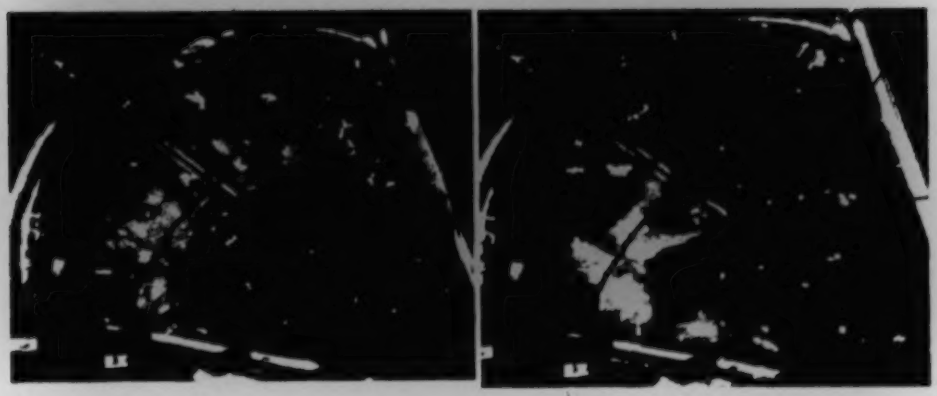

Figure 3.2: An example of an unsteady flow pattern. For this experiment, $\Omega = 0.5\,s^{-1}$, $S = 1.67\,\mathrm{cm^3 s^{-1}}$, $m_b = 0.033$, and, the source-sink distance was 6 cm.

### c) Impact of the source-sink distance on the flow pattern

In experiments in which the sink was placed at different distances from the fixed source location the resulting flow pattern was strongly dependent on the source-sink distance.

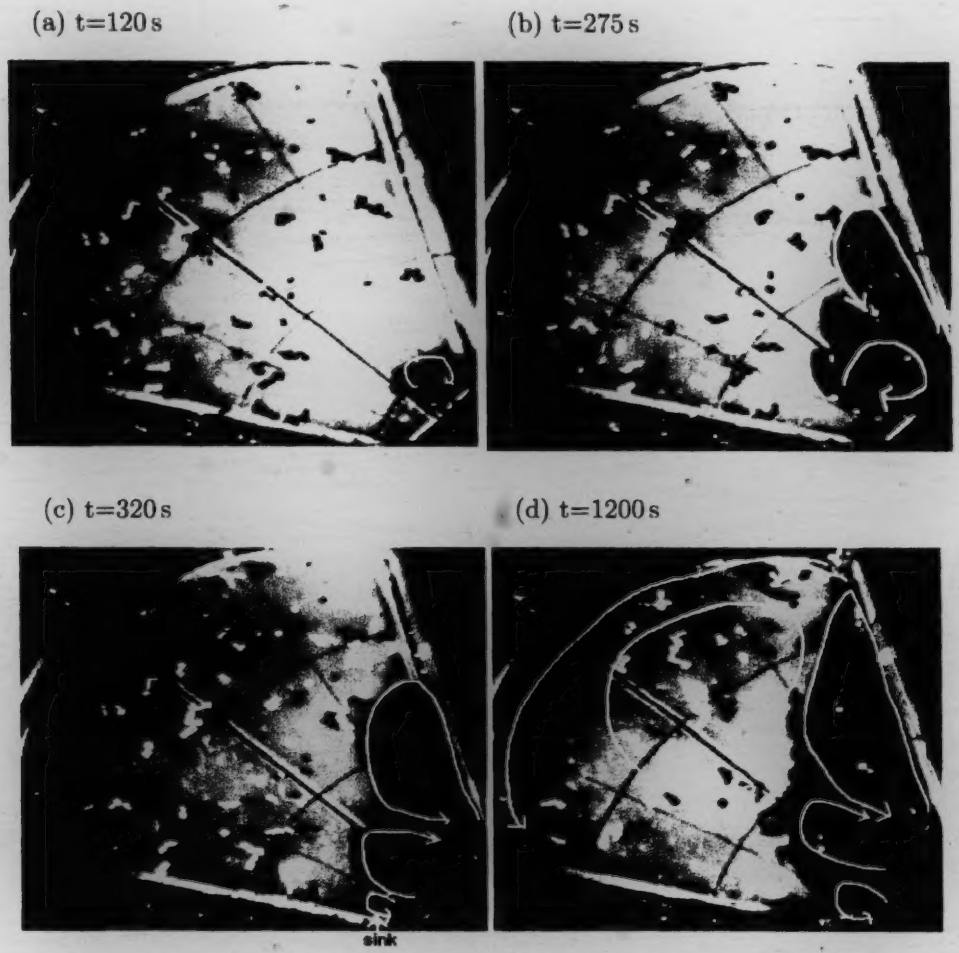


Figure 3.3: Examples of flow patterns when the source was placed in 6 cm from the source. For this experiment, $\Omega = 1.05\,s^{-1}$, $S = 1.33\,\mathrm{cm^3 s^{-1}}$, $m_b = 0.033$.

When the sink was 6 cm from the source, the emerging fluid, under the influence of rotation, flowed to the right and formed a stationary clockwise circulation, as viewed from above, near the apex (Fig. 3.3a). Due to the counterclockwise rotation of the table the present set-up simulated the northern hemisphere. A clockwise circulation in northern hemisphere is associated with a high pressure centre. The high pressure centre grew in size until injected fluid reached the western wall, after which a boundary current along the western wall formed (Fig. 3.3b). 320 s after injection, and under the influence of the sink's extraction, a low pressure, counter-clockwise circulation developed near the eastern wall (Fig. 3.3c). Visualization of this circulation around the sink was soon smeared by the accumulation of dyed fluid injected from the source. A fourth circulation pattern was induced in the interior of the basin almost at the same time that fluid reached the southern wall. This circulation was counterclockwise and interacted with the other two (larger) circulations. When the fluid reached the end of the western wall, it flowed along the southern wall forming a zonal current (although this was very weak; Fig. 3.3d).

When the sink was placed 55 cm from the source, the flow pattern was quite different (Fig. 3.4). The initial counterclockwise circulation (Fig. 3.4a) and western boundary flow (Fig. 3.4b) were similar to the previous case. The flow advanced smoothly along the western wall until it reached the southern wall (Fig. 3.4c) at which point it developed a strong zonal flow along the southern wall (Fig. 3.4d).

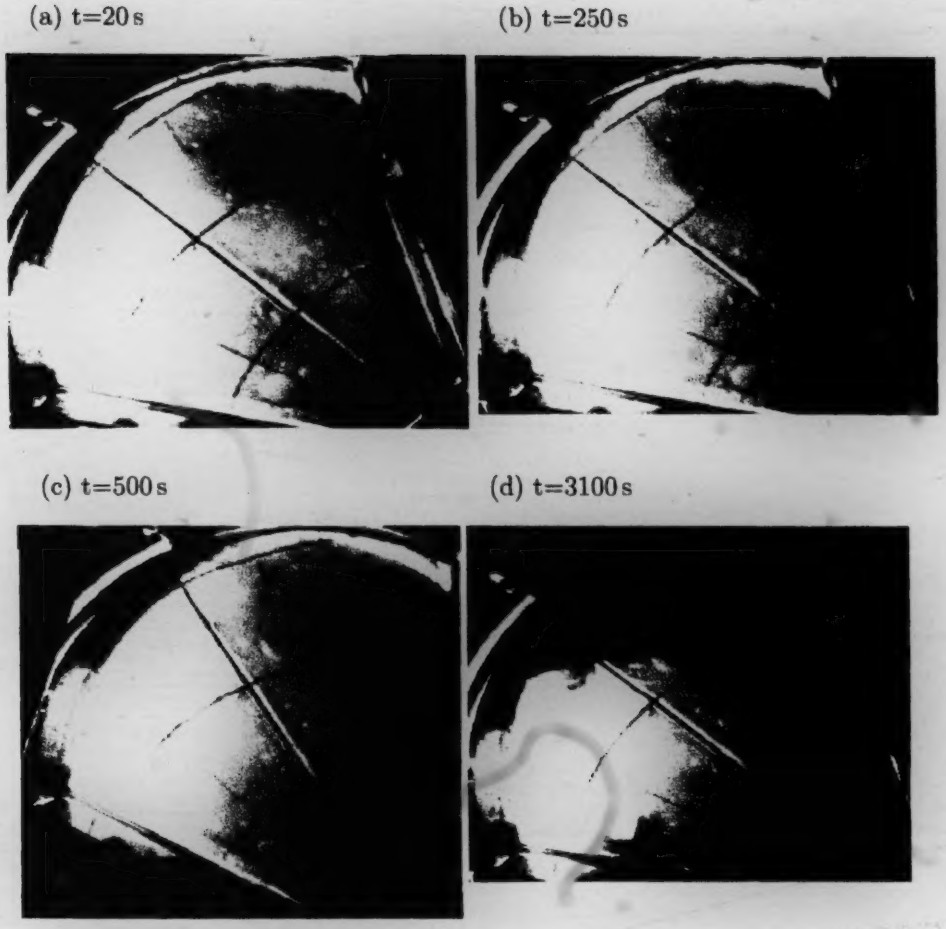


Figure 3.4: Examples of flow patterns when the source was placed in 55 cm from the source. For this experiment, $\Omega = 1.05\,s^{-1}$, $S = 1.33\,\mathrm{cm}^3\mathrm{s}^{-1}$, $m_b = 0.033$.

### 3.1.2 Replication of ST58

To compare the results of our work with ST58 we had to estimate their experimental parameters from what information was given. By calculating the

boundary current width and velocity (from the first panel of Fig. 8 in ST58), we were able to treat the data from their work in the same way as our own. However, since the ST58 tank bottom is level, we calculated the water surface deflection (slope), at $r = a$, (where $a$ is the radius of their tank, approximately 100 cm) caused by the rotation of their tank from equation (2.4) and used it as an equivalent for the bottom slope. Other information, including velocity and width of the flow, the average volume of water in the tank (since volume was not constant in their work), the maximum height, source strength and rotation rate in ST58 were found from their tables and graphs. In summary, we used 0.09 cm for the boundary current velocity, 1.5 cm for the boundary current width, $2\,\mathrm{cm^3 s^{-1}}$ for the flow rate, $1.05\,\mathrm{s^{-1}}$ for the rotation rate, 12 cm for the average maximum height of water in the tank, and 0.11 (an average of surface slope induced by rotation given by (2.4)) for the bottom slope. We found all these numbers to be within the range of our experimental parameters and data.

Fig. 3.4d shows a snapshot of an experiment that was done to replicate the ST58 work. A comparison between Fig. 3.4d and the original work of ST58 (shown in the second panel of Fig. 8 in ST58) shows that the basic features are similar. Both figures show a smooth boundary current with a zonal flow along the southern wall. In Fig. 3.5, the time series taken along the bisector of the apex angle shows advancement of the interface between dyed fluid and ambient fluid at the southern wall. From t= 1500 s to $t$=2800 s this interface moved toward the apex. After this time, however, the interface stopped and no more

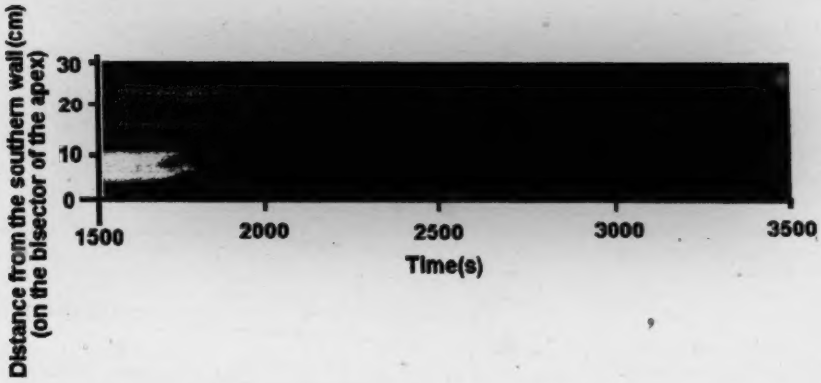


Figure 3.5: Time series taken from the experiment in which the ST58 work was replicated. It shows the motion of the interface of the dyed fluid with the ambient as advancing on the bisector of the apex angle. The experimental parameters are the same as Fig. 3.4

advancement was seen. This is contradictory to the schematic drawn in ST58 (Fig. 3 in ST58) from which they concluded that there must be a northward (toward the apex) motion from the southern wall that extends throughout the tank from the southern wall to the apex. It is also seen here that the motion of the interface is not a steady linear one as the ST58 schematics imply.

We were not able to calculate $\lambda$ for ST58 since there was no reliable information about the technique by which they injected the fluid into the tank.

## 3.2 Second series (Baroclinic mode)

A total of 22 experiments were done in the second series of experiments, of which 5 were discarded due to technical problems. Since, in this series, the injected fluid was denser than the ambient fluid, the vertical structure of the flow was not homogeneous and the flow was potentially "baroclinic." In the second

series of experiments, it was decided to incorporate the bottom slope in such a way that the linear slope of the bottom topography was at least an order of magnitude greater than the parabolic deflection of the water surface caused by rotation. This procedure leads to an approximately constant and uniform value for $\beta$ in each experiment. The greatest technically achievable bottom slope was 0.13. This slope imposed an upper bound of 0.5 $s^{-1}$ on the rotation rate $\Omega$.

Both numerical studies (Sutyrin et al., 2001; Choboter and Swaters, 2000 among others) and observations (Lozier, 1997 and Arhan et al., 2002 among others) suggest that a dense boundary current becomes unstable under certain conditions such as if the Burger number of the flow is smaller than 0.76 (according to Eady linear instability model, (Eady, 1949)) or when the available potential energy is converted to kinetic energy which causes a significant growth in the amplitude of the initially small perturbations. Therefore, to have a more realistic understanding of the boundary flow, the main goal in the second series of the experiments was to produce and examine a variety of flow patterns in the tank and to determine whether we could find a single parameter with which to classify the flow regimes.

### 3.2.1 Basic fluid motion patterns

A number of sensitivity experiments were performed that explored the impact on the flow of the bottom slope $m_b$, fluid height $H_T$, rotation rate

$\Omega$,density difference $\Delta\rho$, and nozzle surface area $A_n$.

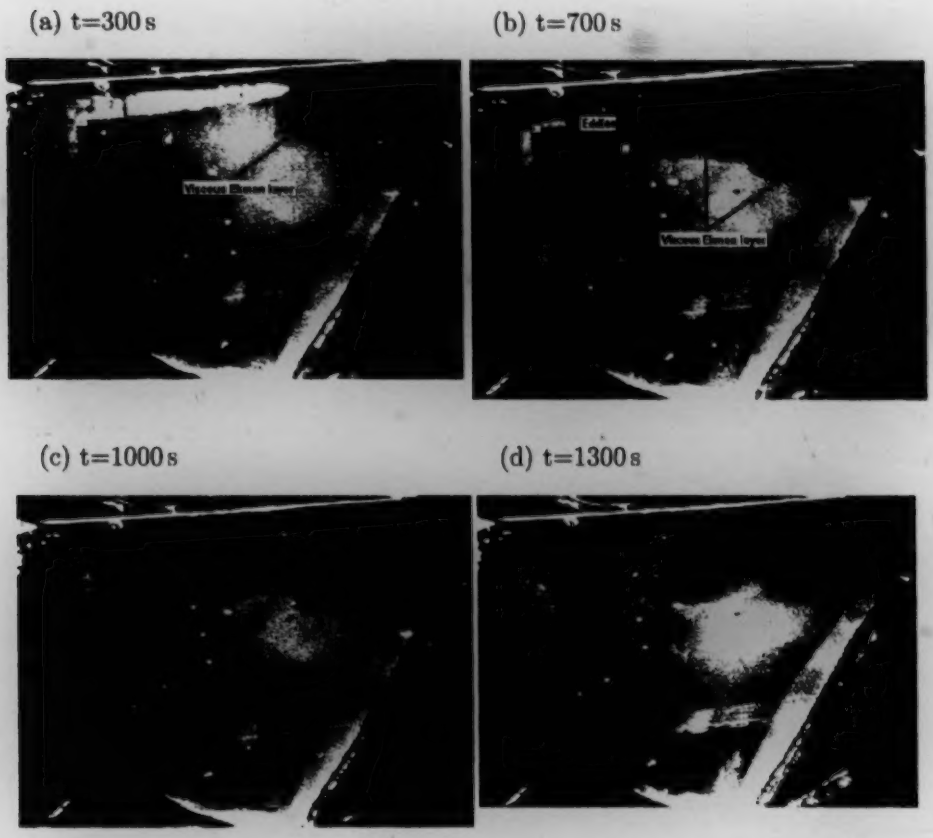


Figure 3.6: Snapshots from a reference experiment with a flow pattern consisted of an eddies' train. For this experiment, $\Delta\rho = 0.007\,\mathrm{g\,cm^{-3}}$, $\Omega = 0.5\,s^{-1}$, $S = 0.17\,\mathrm{cm^3 s^{-1}}$ and $m_b = 0.13$.

In all of the experiments, the western boundary flow did not extend from the bottom to the top of the ambient fluid as in the barotropic series. Rather it was confined to a depth which, for a constant rotation rate and flow rate, was determined mainly by the density difference between the injected fluid and the ambient fluid such that the depth of the current decreased with an increase

in the density difference. Higher boundary current velocities were observed in comparison with the "barotropic" experiments. In all cases, the surface circulation pattern was similar to, but stronger than, the barotropic anticyclonic and cyclonic circulations near the source and sink, respectively.

The observed flow patterns consisted of a train of eddies propagating along the western wall (Figures. 3.6a-d). We defined a nondimensional parameter in a similar way to that of the first series, noting that the appropriate "deformation length scale" had to be different since in a baroclinic system, buoyancy forces are important. This "deformation length" is best described by the Rossby deformation radius, defined as:

$$L_D = \sqrt{g' H_T}/f. \tag{3.2}$$

Hence in the second series of experiments we scaled eddy radius by $L_D$, which is typically much bigger (an order of magnitude or two) than the observed eddies. The nondimensional parameter $\lambda'$ therefore is:

$$\lambda' = log_{10} \frac{S}{{L_D}^3 f m_b}, \tag{3.3}$$

where, due to the smallness of $\frac{S}{{L_D}^3 f m_b}$, we took the logarithm. $\lambda'$ ranged between -2.07 and -3.93. Note that here $\lambda'$ is again the ratio of the time scale associated with topographic-$\beta$ to that of the vortex formation.

In experiments with larger $S$ the flow patterns were more turbulent and

Ekman layers associated with each eddy were wider. On the other hand, in the experiments with high rotation rate the Ekman layer was narrower as a result of the increase in rotation rate.

### 3.2.2 Impact of $m_b$, $A_n$ and $H_T$ on the flow pattern

Two experiments were performed with a bottom slope of 0.065 while all other parameters were kept the same. The resulting flow pattern consisted of a series of eddies in both experiments. Eddies in these cases were dome-shaped. The height of the dense boundary current remained nearly unchanged when the rotation rate was high (i.e. when $\Omega = 0.5\,s^{-1}$) but was almost doubled in the experiment with lower rotation rate. In experiments with larger bottom slope the eddies propagated at a lower velocity.

In experiments with smaller nozzle area ($A_n$= 0.05 cm$^2$) the flow pattern was much more turbulent in both experiments. The dyed dense fluid was mixed with the ambient fluid much more than in the other experiments and caused more vertical extension of the injected fluid. The height of the boundary current was higher than other experiments and decreased slightly along the western wall as the flow moved away from the source of the turbulence (the nozzle).

There was little difference in the flow pattern when the maximum depth $H_T$ was increased.

# Chapter 4

# Quantitative results

In this chapter the quantitative results for both series will be explained in terms of the nondimensional parameters.

## 4.1 First series

For the first series an "injection" length scale, $L$, defined as $\frac{v_n}{f}$, was used to scale the boundary current width, $W_b$. Here $v_n$ is the velocity at which fluid is injected at the source. $L$ is therefore a measure of the distance travelled by the injected fluid during one rotation of the tank.

We also defined a velocity scale, $\beta L^2$, which was used to scale the boundary current velocity.

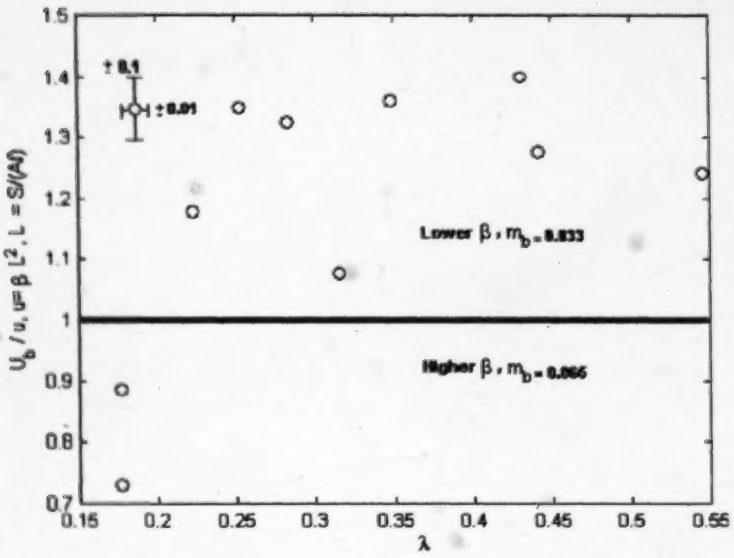


Figure 4.1: Nondimensional boundary current velocity versus $\lambda$.

**a) Scaled boundary current velocity.**

In Fig. 4.1 the scaled boundary current velocity is plotted versus $\lambda$ as defined in eq. (3.1). $\beta L^2$ seems to be an appropriate velocity scale since all cases have nondimensional velocities relatively close to unity. Cases with a bottom slope $m_b$=0.033 (above the solid line) have values greater than unity and cases with an increased bottom slope (below the solid line) correspond to values smaller than unity. This is an indication of the impact of topographic-$\beta$ on the flow, such that increasing $\beta$ decreases the scaled flow velocity. There is no apparent trend seen in Fig. 4.1. Note that cases with smallest value of $\lambda$ correspond to the cases with an increase in the bottom slope (hence topographic-$\beta$) which apparently led to a decrease in the nondimensional velocity.

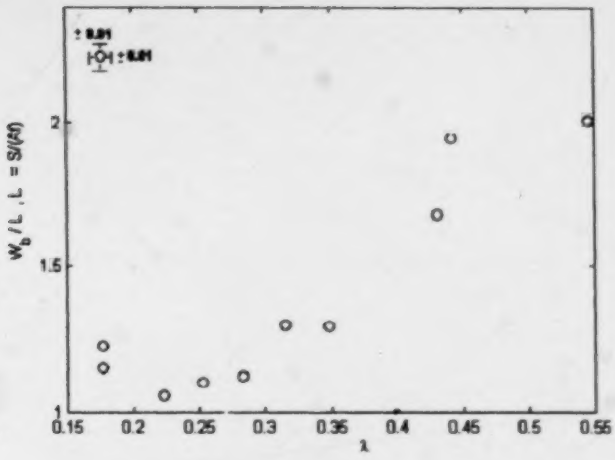


Figure 4.2: Nondimensional boundary current width versus $\lambda$.

**b) Scaled boundary current width.**

In Fig. 4.2 the scaled boundary current width is plotted versus $\lambda$. All the points are of the same order of magnitude and close to unity. This indicates the relevance of the chosen length scale. The positive trend seen in the Fig. 4.2 shows that as the time scale associated with the topographic-$\beta$, $\tau_b$ dominates over the time scale associated with vortex formation, $\tau_v$, (i.e., $\lambda$ increases) the nondimensional boundary current width increases. Note that two cases with increased bottom slopes (hence enhanced topographic-$\beta$) have the smallest values of $\lambda$ and are among the points with smaller nondimensional boundary current width. It is also implied from the Fig. 4.2 that $L$ scales the boundary current width when the $\tau_b \ll \tau_v$.

## 4.2 Second series

For the second series the deformation radius, $L$, defined as $\frac{(g' H_T)^{\frac{1}{2}}}{f}$ was used to scale the eddy radius $r_e$. $L$ is also the Rossby radius of deformation. Similar to the first series, we also defined a velocity scale as $\beta L^2$ which was used to scale the eddy velocity.

**a) Scaled eddy velocity**

In Fig. 4.3 the scaled eddy velocity is plotted against $\lambda'$. Two regions can be seen in this graph. In the first region (to the left of the solid line) the eddy radius, $r_e$ is much smaller than the corresponding Rossby deformation radius, $L_D$. This region is also marked by relatively small nondimensional velocity values (typically 0.05). To the right of the solid line $r_e$ is comparable to $L_D$. In this region nondimensional velocities are considerably larger than those of the first region. In fact we can see that there is a trend from slower eddies toward faster ones as $\lambda'$ increases with a sudden jump across the solid line at $\lambda' \simeq -2.9$.

**b) Scaled eddy radius**

In Fig. 4.4 the scaled eddy radius is plotted against $\lambda'$. As in Fig. 4.3 two regions are formed at approximately the same $\lambda'$ (-2.9). The same trend is also seen in this graph; as $\lambda'$ increases, the eddies' sizes become larger. We can see that in both regions eddies' sizes are much smaller than $L_D$. Since the boundary current width is typically comparable to the eddy radius all the observed

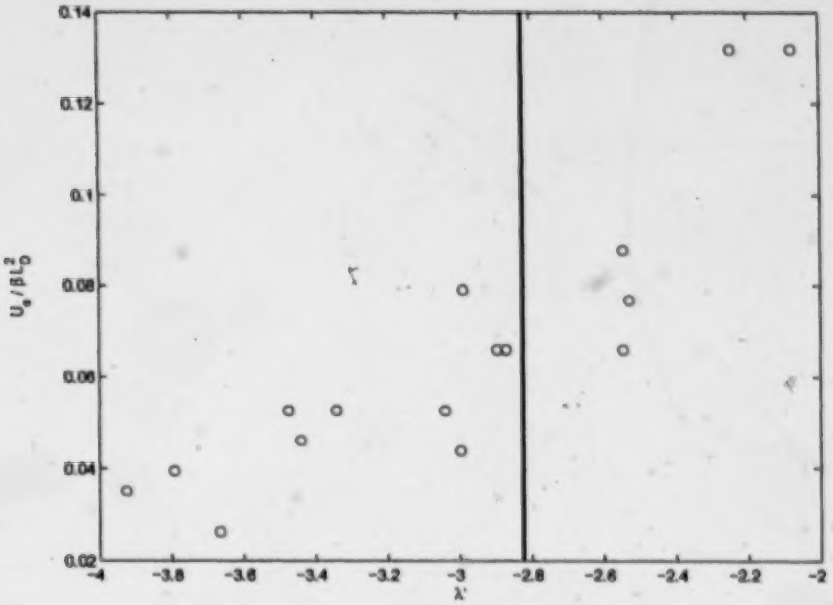


Figure 4.3: Nondimensional eddy velocity versus $\lambda'$.

boundary flows had length scales smaller than the Rossby radius of deformation. Since the length scale of the eddies are smaller than the deformation radius it is unlikely that they arise from baroclinic instability. In the next section we examine the origin of the eddies using the "subcritical slope" theory of N02. Note that in Fig. 4.4 similar to Fig. 4.2 as $\tau_b$ dominates over $\tau_v$ nondimensional size of the eddy increases.

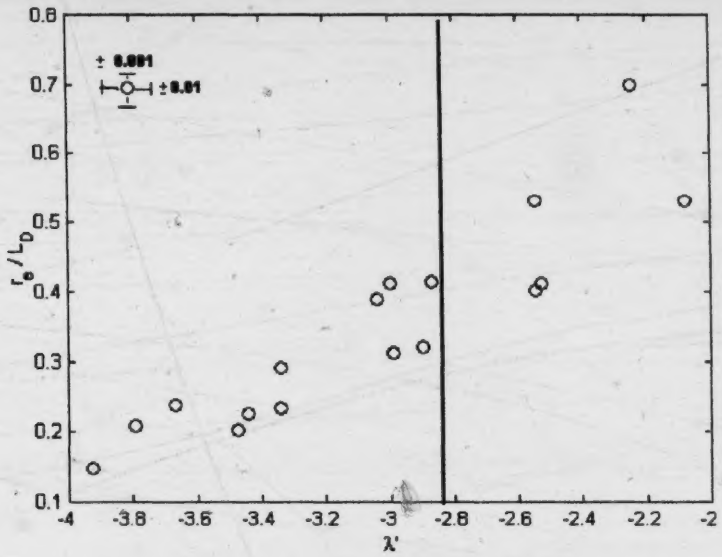


Figure 4.4: Nondimensional eddy radius versus $\lambda'$.

**c) Subcritical slope theory, N02.**

In discussing the origin of Reddy formation, N02 suggest that the slowly varying bottom topography of the Red Sea reaches a critical slope on which the flow can only exist as a train of eddies. It is concluded then that baroclinic instability does not play an important role in the formation of Reddies since mathematically no outflow current can exist to undergo baroclinic instability (see N02 for more detail). This theory is supported by both analytical and numerical analyses (N02). The threshold of this slope is determined from the ratio of the Nof speed (which is the propagation speed of an anticyclonic isolated eddy along lines of constant depth and is defined as $c_n = \frac{g' m_b}{f}$ where we used our own notation; see Nof (1983) for more detail) to the gravity current speed.

(a) Boundary current velocity versus Coriolis parameter, $f$.

(b) Eddy propagation velocity versus Coriolis parameter, $f$.

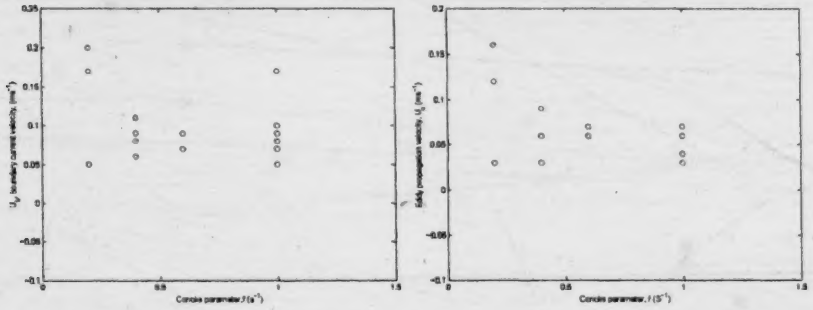

Figure 4.5: Boundary current and eddy propagation velocities versus Coriolis parameter, $f$. $U_b$ is the velocity of that part of the flow which is closest ($\simeq 0.5\,cm$) to the western wall.

This criterion can be written as

$$\lambda_n = \frac{g' m_b / f}{\alpha (g' H_d)^{1/2}}, \tag{4.1}$$

where $\lambda_n$ is notation that we have chosen in analogy with our $\lambda$, $m_b$ is the bottom slope (in our notation), $\alpha$ is $\sqrt{2}$ for a zero potential vorticity flow (a flow with linear, along-isobar velocity profile (i.e., $u{=}fy$ and $y$ is the position of the flow in the cross-isobaric direction) and unity for a uniform potential vorticity flow (a flow with a potential vorticity $P{=}f/H_d$) and $H_d$ is the maximum thickness of the dense flow. Since there is not enough information about the dependency of flow velocity ($U_b$ or $U_e$) on $f$ (Fig. 4.5), in our work we checked both zero and uniform potential vorticities for eddies. Upon calculating $\lambda_n$ for all cases, we found that our experiments had a bottom slope that was subcritical.

The length scale defined in N02 to be the radius of the eddy which is propagating along a subcritical slope is, using our notation,

$$R_n = \sqrt[3]{\frac{32S}{\pi m_b f}}. \tag{4.2}$$

In deriving (4.2), N02 supposed that the zero potential vorticity eddy is translating along isobaths (across the slope) at the Nof speed ($c_n$) and has a volume of $\frac{\pi f^2 r_e^4}{16g'}$ (where we used or own notation; see N02 for more detail).

Based on this $R_n$ a velocity scale may be defined as $U_n = \beta R_n^2$.

In Fig. 4.6, the eddy radius scaled by $R_n$ is plotted versus $\lambda_n$. No trend is seen in this graph but the points are closer to unity than they are when the Rossby radius of deformation, $L_D$, is used as the relevant length scale (Fig. 4.4). Cases with a decrease in bottom slope, $m_b$, and nozzle surface area, $A_n$, or an increase in height, $H_T$, are seen among the points above the solid horizontal line. We can see that in cases with increased $H_T$, or decreased $m_b$, topographic-$\beta$ is decreased hence the scaled eddy size is increased which is in agreement with the physics of the phenomena. In flows with a smaller nozzle surface area the scaled eddy radius increased as a consequence of enhanced turbulent mixing.

Fig 4.7 shows eddy velocity, scaled by $U_n$, versus $\lambda'$. $U_e$ and $U_n$ are of the same order of magnitude. Most of the eddies formed in the region with small $\lambda_n$. $R_n$ and $U_n$ are therefore an appropriate set of scales for our experiments. This implies that our experiments have been done in Nof's regime in which

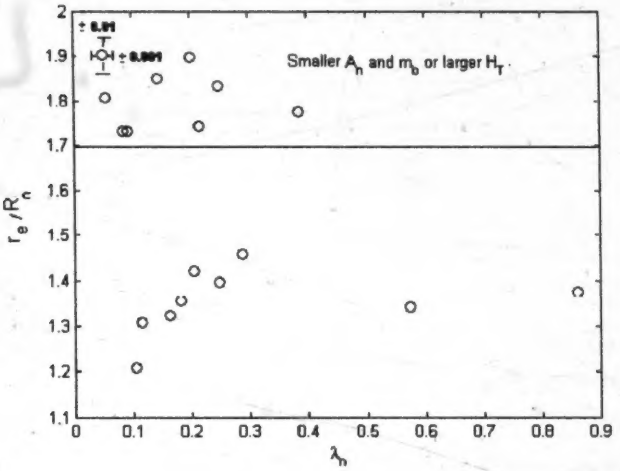


Figure 4.6: Eddy radius scaled by $R_n$ versus $\lambda_n$.

baroclinic instability does not play much of a role in the formation of eddies. From time series and direct observation we can say that we found no evidence of a boundary current which underwent baroclinic instability. Instead the dominant mechanisms in eddy formation in our experiments were vortex stretching in the upper layer and Rossby wave propagation towards the western wall. Eddies formed near the nozzle due to upper layer vortex stretching, they migrated to the western wall due to the topographic-$\beta$ effect and this cycle was repeated to form a series of eddies propagating along the western wall. This procedure is proposed as the dominant mechanism for eddy formation by both LB98, Cenedese et al. (2003), and Elting et al. (2000) (in the first series of their experiments) which is consistent with our experimental results.

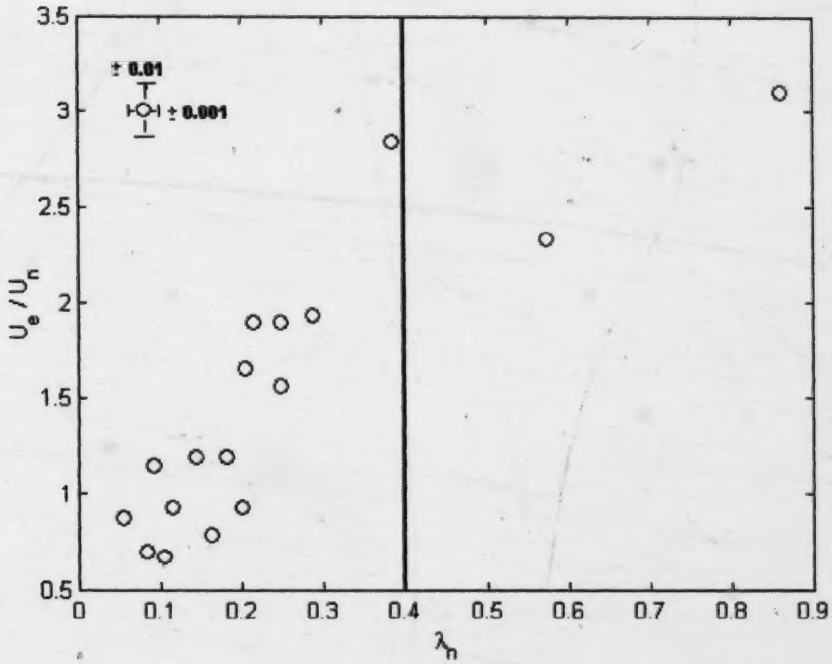


Figure 4.7: Eddy velocity scaled by $U_n$ versus $\lambda_n$.

# Chapter 5

# Conclusions

In the present work benthic oceanic flows were simulated experimentally. These simulations were done in two major sets. In the first series the vertical structure of the simulated ocean was assumed to be homogeneous, hence the flows were barotropic. In the second series the vertical structure of the simulated ocean was not homogeneous and consisted of a dense fluid injected from the source into an ambient fluid that was fresh water; hence the second series is baroclinic. Flow patterns in the barotropic experiments were classified into two main types: quasi-steady and unsteady. Threshold criterion in terms of a single parameter, $\lambda$, were found. $\lambda$ is the ratio of two different timescales: one of order $(\beta L)^{-1}$, (or reciprocal of the Rossby wave frequency) corresponding to the time required for a fluid parcel to enter the boundary current by Rossby wave propagation, and the other one of order $\frac{V_v}{S}$, where $V_v$ is a measure of the volume

of the vortex formed in the vicinity of the source of strength $S$. With this threshold parameter we managed to classify the flows consistently in a certain interval. It was shown that for larger values of $\lambda$ flows were more steady whereas for smaller values of $\lambda$ the flows tend to be more unsteady. We also compared our results with the ST58 work. While we managed to replicate their work with a different set-up and found some similar features, there were some differences as well. For example, we could find no uniform return flow towards the apex in a case that was identical to theirs. Although there was net motion towards the apex, it was not uniform motion like in their schematics this could be due to the radius dependent $\beta$ that they used. Using time series produced with Digimage we found that fluid particles in the bulk of the ambient did not move in a consistently radial direction and in particular they did not reach the apex even after 1.5 hours. Comparison with ST58 should be done cautiously since the lack of reliable information about the mechanism of fluid injection in their experiments did not allow us to calculate the corresponding $\lambda$ for their work.

Similar to the barotropic flows, we also classified our baroclinic flows in terms of another nondimensional parameter $\lambda'$ which was based on the Rossby radius of deformation. All the flows were essentially the same in a sense that a series of eddies were formed. It was also found that all eddies are smaller than the Rossby radius of deformation. Since the spatial scales of the boundary current and eddies were typically the same we concluded that the boundary current did not undergo baroclinic instability. Instead, vortex stretching and Rossby wave

propagation mechanisms were found to be the active mechanisms. It was shown that for larger $\lambda'$ the Rossby radius of deformation is a more relevant length scale.

We also verified the "subcritical slope" hypothesis suggested by N02. Our results indicate that all cases in our work were on the "subcritical slope".

Like LB98, we found that the Nof speed is not the relevant velocity scale. Instead a Rossby wave propagation speed based on the eddy size defined in N02 was found to be the appropriate velocity scale.

For the future research we suggest the following ideas. In the barotropic mode of the work we did not study the return flow from the southern wall in detail. In fact, the present set-up were designed in such a way that only the dynamics of the boundary current could be examined in detail. In a different set-up the return flow could be studied in more detail. Also the baroclinic experiments could be extended to include a multi layered environment, where the impact of stratification on the eddy formation process can be studied in more detail.

# Bibliography

Alverson, K. and Owens, W. (1996). Topographic preconditioning of open ocean deep convection. *J. Phys. Oceanogr.*, **26**:2196-2213.

Apel, J. R. (1990). *Principles of Ocean Physics.* Academic press.

Arhan, M., Carton, X., Piola, A. and Zenk, W. (2002). Deep lenses of circumpolar water in the argentine basin. *J. Geophys. Res.*, **107** (C1):1029-1040.

Broecker, W. S. (1991). The Great Ocean Conveyor. *Oceanography*, **4**, 79-89.

Cessi, P. R., Condie, R. V. and Young, V. R. (1990). Dissipative dynamics of western boundary currents. *J. Marine Res.*, **48**:677-700.

Choboter, P. F. and Swaters., G. E. (2000). On the baroclinic instability of axisymetric rotating gravity currents with bottom slope. *J. Fluid. Mech.*, **408**:149-177.

Condie, S. A. (1995). Descent of dense water masses along continental slopes. *Journal of Marine Research*, **53**:865 – 928.

Dalziel, S. B. (1993). Rayleigh-Taylor instability: experiments with image analysis. *Dyn. Atmos. Oceans*, **20**:127-153.

DiBattista, M. T., Majda, A., Marshall, J. (2002). A statistical theory for the "patchiness" of open- ocean deep convection: The effect of preconditioning. *J. Phys. Oceanogr.*, **32**:599-613.

Eady, E. (1949). *Tellus*, **1**:33-52

Egbert, G. D. and Ray, R. D. (2000). Significant dissipation of tidal energy in the deep ocean inferred from satellite altimeter data. *Nature*, **405**:775-778.

Etling, D., Gelhardt, F., Schrader, U., Chaber d' Hières, G., Brennecke, F., Kuehn, G. and Didelle, H. (2000). Experiments with density currents on a sloping bottom in a rotating fluid. *Dyn. Atmos. Oceans*, **31**: 139-164.

Gill, A. E. (1982). *Atmosphere-Ocean Dynamics*. Academic Press.

Griffiths, R. W. and Linden, P. W. (1982). Laboratory experiments on fronts. Part 1: Density-driven boundary currents. *Geophysical and Astrophysical Fluid Dynamics*, **19**:159 – 187.

Hendershott, M. C. (1987). *General Circulation of the Ocean*. Springer.

Ierely, G. R. (1987). On the onset of recirculation in barotropic general circulation models. *J. Phys. Oceanogr.*, **17**:2366-2374.

Ierely, G. R. and Reuher, O. G. (1986). Analytical and numerical solutions of a nonlinear boundary-layer problem. *Studies in App. Math.*, **75**:1-36.

Ierely, G. R. and Sheremet, V. (1995) Multiple solutions and inertial runaway of the wind driven circulation. *J. Mar. Res.*, **53**:703-737.

Killworth, P. (1998). Something steers in the deep. *Nature*, **369**:720-721.

Lanes-Serff, G. F. and Baines, P. G. (1998). Eddy formation by dense flow on slopes in a rotating fluid. *J. Fluid. Mech.*, **363**:229-252.

Ledwell, J., Watson A. and Law, C. (1993). Evidence for slow mixing across the pycnocline from an open-ocean tracer-release experiment. *Nature*, **346**:701-703.

Lozier, M. S. (1997). Evidence for large-scale eddy-driven Gyres in the North Atlantic. *Science*, **277**:361-364.

Madec, G., Lott, F. Delecluse P. and Crepon, M. (1996). Large-scale preconditioning of deep-water formation in the northwestern Mediterranean Sea. *J. Phys. Oceanogr.*, **26**:1393-1408.

Morgan, G. W. (1956). On the wind-driven ocean circulation. *Tellus*, **8**:301-320.

Munk, W. H. (1950). On the wind driven ocean circulation. *J. Meteor.*, **7**:79-93.

Niiler, P. P. (1987). *General Circulation of the Ocean.* Springer.

Nof, D. (1983). The translation of isolated cold eddies on a sloping bottom. *Deep-Sea Res. I*, **30**:171 – 182.

Nof, D., Paldor N. and Van Gorder, S. (2002). The Reddy maker. *Deep-Sea Res. I*, **49**(9):1531-1549.

Pedlosky, J. (1987). *Geophysical Fluid Dynamics*. Springer.

Pedlosky, J. (1996). *Ocean Circulation Theory*. Springer.

Reszka, M. K. Swaters, G. E. and Sutherland,B. R. (2002). Instability of Abyssal Currents in a Continuously Stratified Ocean with Bottom Topography. *J. Phys. Oceanogr.*, **32**: 3528-3550.

Rhines, P. B. (1975). Waves and turbulence on a beta plane. , **69**:417-443.

Stewart, R. H. (2003). Introduction To Physical Oceanography. Department of Oceanography Texas A & M University.

Stommel, H., Arons, A. and Faller, A. (1958). Some example of stationary planetary flow patterns in bounded sea. *Tellus*, **10**:179-187.

Stommel, H. and Arons, A. (1960). On the abyssal circulation of the world ocean-I. Stationary planetary flow pattern on a sphere. *Deep-Sea Res.*, **6**:140-154.

Streeter, V. L. (1971). *Fluid Mechanics*. McGraw-Hill.

Sutyrin, G., Rowe, D., Rothstein, L. and Ginis, I. (2003). Baroclinic-eddy interactions with continental slopes and shelves. *J. Phys Oceanogr.*, **33**:283-291.

Swaters, G. E. (1991). On the baroclinic instability of cold-core coupled density fronts on a sloping continental shelf. *J. Fluid Mech.*, **224**:361-382.

Tansley, C. T. and Marshall, D. P. (2001). Flow past a cylinder on a $\beta$ plane, with application to Gulf stream separation and the Antarctic circumpolar current. *J. Phys. Oceanogr.*, **31**:3274-3283.

Voropayev, S. I., Zhang, X., Boyer, D. L., Fernando, H. J. S. and Wu, C. W. (1997). Horizontal jets in a rotating fluid. *Phys. Fluid.*, **9** (1):115-126.